D³He-proton emission imaging for inertial-confinement-fusion experiments (invited)

F. H. Séguin,[a] J. L. DeCiantis, J. A. Frenje, S. Kurebayashi, C. K. Li, J. R. Rygg, C. Chen, V. Berube, B. E. Schwartz, and R. D. Petrasso[b]
Plasma Science and Fusion Center, Massachusetts Institute of Technology, Cambridge, Massachusett 02139

V. A. Smalyuk, F. J. Marshall, J. P. Knauer, J. A. Delettrez, P. W. McKenty, D. D. Meyerhofer,[c] S. Roberts, and T. C. Sangster
Laboratory for Laser Energetics, University of Rochester, Rochester, New York 14623

K. Mikaelian and H. S. Park
Lawrence Livermore National Laboratory, Livermore, California 94550

Proton emission imaging cameras, in combination with proton spectrometers and a proton temporal diagnostic, provide a great deal of information about the spatial structure and time evolution of inertial-confinement fusion capsule implosions. When used with D³He-filled capsules, multiple proton emission imaging cameras measure the spatial distribution of fusion burn, with three-dimensional information about burn symmetry. Simultaneously, multiple spectrometers measure areal density as a function of angle around the imploded capsule. Experiments at the OMEGA laser facility [T. R. Boehly *et al.*, Opt. Commun. **133**, 495 (1997)] have already proven the utility of this approach. An introduction to the hardware used for penumbral imaging, and algorithms used to create images of the burn region, are provided here along with simple scaling laws relating image resolution and signal-to-noise ratio to characteristics of the cameras and the burn region. © *2004 American Institute of Physics.* [DOI: 10.1063/1.1788892]

I. INTRODUCTION

Understanding and controlling implosion dynamics are critical for progress in inertial-confinement-fusion (ICF), where achieving spherical symmetry in the assembled fuel mass is a prerequisite for optimal burn and ignition.[1–3] It is therefore important to have direct experimental observations of what implosion asymmetries look like, how they evolve, and how they are correlated with sources of asymmetry such as illumination nonuniformity. Traditional methods of studying asymmetry include x-ray imaging,[4] neutron-emission imaging of deuterium-tritium (DT) burn,[5–26] and measurement of primary or secondary D³He proton spectra for determining the areal density (ρR) of capsules at different angles.[27–31] We report here an integrated approach to studying dynamics, symmetry, and nuclear burn characteristics in implosions of capsules containing D³He fuel, utilizing three independent but directly related types of diagnostic measurements of the 14.7-MeV protons generated by D³He burn. Multiple proton-emission imaging cameras, viewing an implosion from three orthogonal directions, are now used in conjunction with a proton temporal diagnostic,[32,33] which measures the D³He proton flux as a function of time, and multiple wedge-range-filter spectrometers,[34] which measure high-resolution spectra of the protons at different angles around the capsule. Taken together, they provide three-dimensional information about the spatial distribution of D³He burn, the time evolution of the burn, and the angular distribution of colder material surrounding the burn region.

The proton-emission imaging cameras are described briefly in Sec. II (with more details elsewhere[35]). They are based on the penumbral imaging technique, which is related to pinhole imaging[20,23–25] but involves an imaging aperture much larger than the source; this results in a raw recorded image that must be deconvolved, because structural information about the source is encoded in the image penumbra. The idea of using penumbral imaging to study ICF burn is at least 20 years old,[5] and at least three different algorithms have been used for deconvolution.

The first algorithm involves deconvolution in frequency space, determining the two-dimensional Fourier transform (FT) of the source surface brightness by multiplying the FT of the penumbral image by a deconvolution filter that is the inverse of the FT of the aperture point spread function.[5–8,10–13,15–18] This approach is complicated somewhat by the fact that the FT of the aperture has zeros at a number of frequencies, leading to singularities in the deconvolution filter. The discrete frequencies used in digital processing generally avoid the singularities, but they come close enough to result in large amplification factors for the statistical noise present in all real data. In practice, noise is con-

---

[a]Electronic mail:seguin@mit.edu
[b]Also Visiting Senior Scientist, Laboratory for Laser Energetics, University of Rochester.
[c]Also Departments of Mechanical Engineering and Physics, and Astronomy, University of Rochester.

trolled by usng a Wiener filter approach to modify the ideal deconvolution filter in such a way as to reduce noise amplification near the singularities while minimizing distortion to real structural information in the data. This direct reconstruction approach has been used for DT neutrons[11–19] and for 3-MeV DD protons.[36,37] Another direct reconstruction algorithm that works in frequency space[21] has been applied to DT neutrons.[22] It uses a different approximation to the ideal frequency-space deconvolution filter, obtained by multiplying the aperture FT itself by another nonsingular function of frequency. This algorithm is exact only in the limit where the radius of the source r_s is much smaller than the radius of the imaging aperture R_a, but errors are small for practical ratios r_s/R_a. The implementation is computationally simple and efficient, and no special precautions have to be made for noise reduction other than some kind of low-pass filtering. The third algorithm is iterative rather than direct, and involves computations only in physical space. It utilizes a "maximum entropy" technique to find an estimate for the source surface brightness that has the least possible structure consistent with the structure and the statistical errors of the penumbral image.[9] An initial guess for the source is used to stimulate penumbral image data, and the difference between the real and simulated penumbral images is used to find a more accurate source estimate; the process is repeated until convergence. This approach has been used in imaging with DD protons and DT α particles.[38–41]

Section III describes a different direct, noniterative algorithum involving computation in the spatial domain only. It is computationally efficient, has no issues with filter singularities, and has a well-defined point-response function that allows calculation of simple and explicit scaling laws relating camera parameters and source type to the spatial resolution and signal-to-noise ratio of reconstructed source functions. In addition, the data processing in the spatial domain provides opportunities to see visual connections between data structure and source structure. The method is approximate, with errors scaling as $(r_s/R_a)^2$, but the errors are extremely small for parameters relevant to our applications. A related algorithm, described in Sec. IV, is often used to calculate the radial distribution of reactions per unit volume in the burning source when it can be assumed to have spherical symmetry.

Experiments with D^3He-filled capsules are frequently performed at the University of Rochester OMEGA laser facility,[42] where the techniques described here have been used. D^3He protons are sufficiently energetic to pass through 200 mg/cm^2 of 1-keV plasma (or 1000 mg/cm^2 of a 10-keV plasma), so they are very useful for studying the implosion performance of capsules with thick CH shells that do not allow lower-energy charged particles to escape. These experiments and their significance are described briefly in Sec. V.

II. PROTON EMISSION IMAGING CAMERAS

There are three cameras that can be mounted on the OMEGA target chamber, as shown in Fig. 1(a). Each camera consists of a housing with an aperture at one end and slots
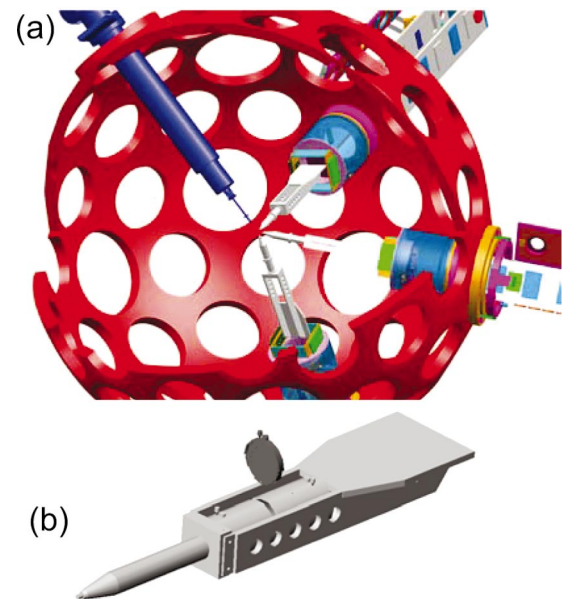

FIG. 1. (Color) Diagrams illustrating the structure of the proton emission imaging cameras. (a) A cutaway view of the OMEGA target chamber, showing three cameras pointed toward the target (located at the chamber center) from nearly orthogonal directions. The structure at 11:00 holds the target capsule in place on its stalk. The diameter of the target chamber is 330 cm. (b) The housing of an individual camera. The aperture is at the left end, and the detector pack (shown in dark gray), is inserted into a slot in the top.

that accept detector packs, as shown in Fig. 1(b). Figure 2(a) shows the approximate dimensions of the cameras. The typical source at OMEGA has a radius of $r_s \sim 30$ μm. The round imaging aperture, at a distance $L \approx 3$ cm from the source, generally has a radius $R_a = 1000$ μm and is cut very accurately in a 500-μm-thick plate of Ta (which will stop protons with energies $\lesssim 17.5$ MeV). The image recorder consists of stacked sheets of CR-39 nuclear track detector separated by ranging filters that result in efficient detection of 14.7-MeV D^3He protons on one sheet and 3-MeV DD protons on another (only D^3He protons will be considered here; other particles will be discussed elsewhere).[35] The parameter M characterizes the magnification of the system.

The CR-39 detectors[43,44] are sheets of a clear plastic in which protons leave trails of damage sites. After etching in NaOH, the entry point of each proton becomes a conical hole that can be identified and quantified in a digitized microscope image. Detection is essentially 100% efficient, as long as the detector has filtering that slows incoming protons down to the range of sensitivity of about 0.5 to 8 MeV, and
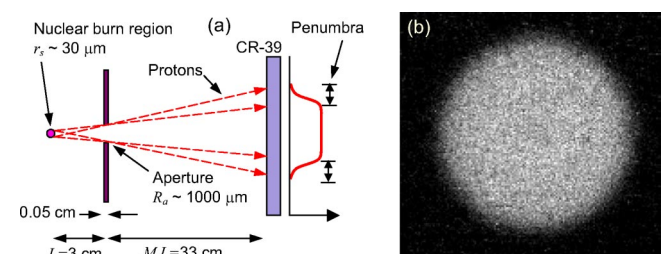

FIG. 2. (Color online) (a) Diagram showing the parameters of a penumbral imaging camera. (b) A sample penumbral image. Brightness is proportional to the number of protons per unit area on the detector.
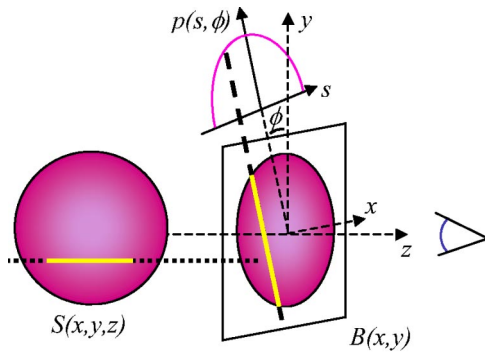
FIG. 3. (Color online) Diagram illustrating the relationship between a three-dimensional source S, the two-dimensional projection B that is its surface brightness, and one-dimensional projections p of B.

the position of each track is recorded to a fraction of a micron. The recorded penumbral image data comprise the precise locations of all proton tracks, which may be binned as desired for any processing scheme. There are therefore essentially no resolution limits imposed by the detector itself.

Resolution degradation from effects such as proton scattering in the target capsule or off the aperture, proton trajectory distortion by electric fields, and geometric distortion due to imperfections in the aperture are all negligible[35] compared to the deliberate degradation of resolution that will have to be imposed on the data through filtering to control statistical noise. For all practical purposes, the aperture can be considered to have a perfect edge in a thin, opaque plate. This allows us to avoid some of the problems that occur in neutron imaging,[13] where even a very thick plate does not stop all neutrons and the aperture "edge" is not as well defined.

A sample proton penumbral image is shown in Fig. 2(b). The number of incident protons per unit area N can be represented as a function of x and y on the detector, or as a function of radius and angle with respect to any position on the detector. The yield of the source can be calculated directly from the value of N in the center of the image (with any background level subtracted): $Y_s = 4\pi(M+1)^2 L^2 N(0,0)$. Information about the source structure must be extracted from the penumbra.

III. SURFACE BRIGHTNESS RECONSTRUCTION

A. Algorithm

Figure 3 shows the relationship between a three-dimensional source function $S(x,y,z)$; its two-dimensional projection along the z axis, which is the surface brightness $B(x,y)$ seen by an observer at positive z; and a one-dimensional projection $p(s,\phi)$ representing straight-line integrals through B at angle ϕ and impact parameters s. The function p is the Radon transform[45] of B, and computationally efficient methods for recovering B from p were developed several decades ago for x-ray computed tomography (CT).[46,47] Although $p(s,\phi)$ cannot be found exactly from a penumbral image, $p(s,\phi) = 4\pi(M+1)^2 L^2 \partial N(r_0 - Ms, \phi)/\partial s$ in the limit where the halfwidth of the penumbra Mr_s is much smaller than the radius $r_0 = (M+1)R_a$ of the aperture as projected on the detector (see Fig. 4). In this limit, standard CT algorithms can be used to reconstruct B from N. When
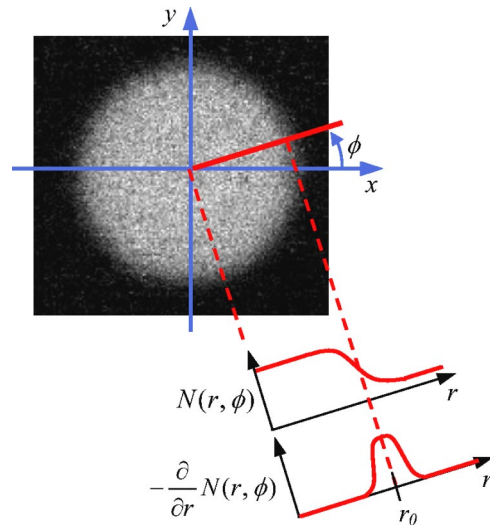

FIG. 4. (Color online) Diagram illustrating the radial profile of N, the number of proton tracks per unit area on the detector, and its radial derivative.

$r_{smax} \equiv r_0/M$ is not large compared to r_s, $\partial N/\partial r$ is approximately proportional to integrals through the source along circular paths with radii r_{smax}. A standard algorithm for CT reconstruction, called convolve-and-backproject or filtered backprojection, can be modified to correct for most of the effects of the curvature as long as $r_s < r_{smax}$. The modified version can be written

$$B(x,y) \approx \frac{1}{2\pi} \int_0^{2\pi} w \mathsf{P}'[R_0 - M(x\cos\phi + y\sin\phi), \phi]d\phi$$
$$- 0.13\, Y_s/\pi r_{smax}^2, \tag{1}$$

where

$$R_0 \equiv \sqrt{r_0^2 - M^2(x\sin\phi - y\cos\phi)^2}, \tag{2}$$

$$w \equiv 1 - M(x\cos\phi + y\sin\phi)/R_0, \tag{3}$$

$$\mathsf{P}(r,\phi) \equiv -[4\pi M(M+1)^2 L^2] C(r)\frac{\partial}{\partial r}N(r,\phi), \tag{4}$$

$$\mathsf{P}'(r,\phi) \equiv F_{conv}(r) * \mathsf{P}(r,\phi), \tag{5}$$

$$F_{conv}(r) \equiv F_{smooth}(r/M) * h_{CT}(r/M). \tag{6}$$

$C(r)$ is a weighting factor described below. P' is found by convolving $\mathsf{P}(r,\phi)$ with a filter F_{conv}, which is a standard CT convolution kernal h_{CT} (we use the version of Ref. 46) convolved with a smoothing filter F_{smooth} discussed below. The integration in Eq. (1) is referred to as backprojection, because it relates structure in the convolved projection back to specific locations in the reconstruction plane.

In the limit $r_s/r_{smax} \ll 1$, Eq. (1) becomes the standard CT reconstruction algorithm described in Refs. 46 and 47: $w = C = 1$, R_0 is a constant, and the term proportional to r_{smax}^{-2} goes to zero. Of the four modifications incorporated here to approximately correct for finite r_s/r_{smax}, the most important is the angular dependence of Eq. (2). This exact correction was derived to guarantee that structure in the projections is

"backprojected" along the correct curved paths through the reconstructed image plane rather than along straight lines. The weighting factor w gives different weights to contributions of different projection angles at each position in the source-image plane, to reduce a small distortion in the point-response function at points far from $x=y=0$. The weighting function $C(r)$ compensates approximately for the small difference between the shapes of projections based on straight-line integrals and curved-line integrals. An expression that works well for symmetric sources is

$$C(r) = (1 - 0.22\ell)\ [(\pi/3)\sqrt{1-\ell^2}/\cos^{-1}(r/2r_0)]^{1.4}, \qquad (7)$$

where $\ell \equiv r/r_0 - 1$; it also produces improved reconstructions for asymmetric sources. Finally, the term proportional to r_{smax}^{-2} corrects for a very small dc offset in the reconstructed image; it is a function of yield only (calculated in advance as described in Sec. II), is independent of position, and amounts to ~3% for $r_s/r_{smax}=0.5$. Other modifications are possible, but accuracy is currently more than satisfactory.

B. Implementation and accuracy

Numerical execution of Eqs. (1)–(6) is straightforward and efficient, following steps illustrated with an example in Fig. 5. The positions of individual proton tracks in the penumbral-image proton data are used to determine $N(r,\phi)$, which we typically bin in a grid with 1° angular bins and M μm radial bins [see Fig. 5(b)]. The gradient in the radial direction is calculated and multiplied by $C(r)$ to produce $P(r,\phi)$, as shown in Fig. 5(c), and then convolved in the radial direction with $F_{conv}(r)$ to produce $P'(r,\phi)$, as shown in Fig. 5(d). Finally, $B(x,y)$ is calculated on a grid of 1 -μm pixels using Eq. (1) [see Fig. 5(e)]. Coarser grids would give faster computation, but keeping the bin sizes small relative to the effective resolution of the final reconstruction (see Sec. III C below) assures that structure is not undersampled and also allows the result to look more like a continuous function.

Binning data in r and ϕ requires reference to an origin in the detector plane. This does not have to be the exact center of the penumbral image; shifting the origin simply results in a reconstructed image with a shifted origin. What does need to be known accurately is the radius r_0. Although it is usually known fairly accurately from design parameters, it can be found directly from the data using the fact that the average over ϕ of $P(r,\phi)$ is symmetric about r_0.

Equation (1) produces reconstructions that are not exactly correct except in the limit $r_s/r_{smax} \ll 1$, but are extremely accurate for the values $r_s/r_{smax} < 0.1$ that are relevant here (amplitude errors less than 0.5%, and perfect positional accuracy). Even for $r_s/r_{smax}=0.5$, simulations show that the positional accuracy is perfect (see Fig. 5) and the amplitude errors are a few percent (see Fig. 6).

The steps involved in performing image reconstruction provide opportunities to see visual connections between data structure and source structure in a satisfying way that is not always possible with frequency-space calculations. The values $P(r,\phi)$ in Fig. 5(c) are approximately the line integrals $p(s,\phi)$ of Fig. 3, where $s \approx (r-r_0)/M$, and an experienced eye can see how the line integrals are related to the source. In
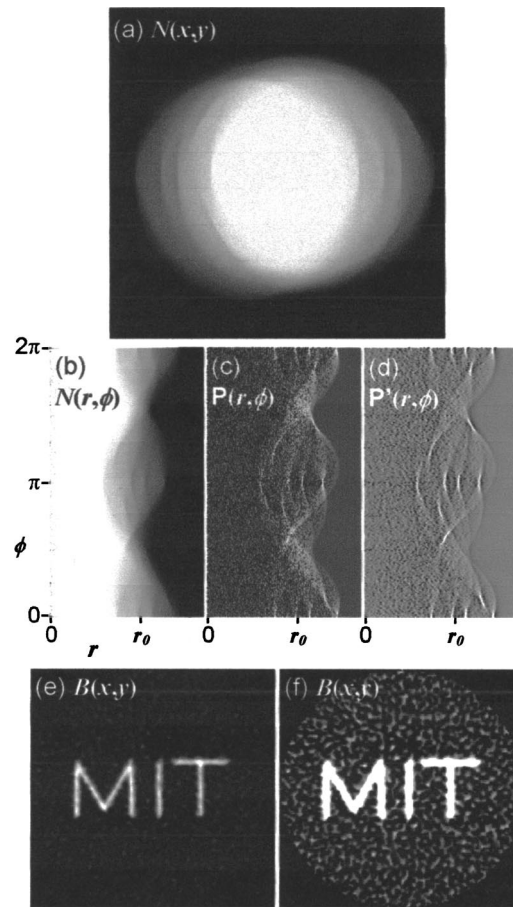

FIG. 5. Simulated penumbral image (a), reconstruction of source surface brightness (e) and (f), and intermediate data-processing steps (b)–(d). $N(x,y)$ was generated by a Monte Carlo program for an assumed $B(x,y)$ containing geometrically precise, short-wavelength information and having a maximum radius of $0.5r_{smax}$. The reconstruction (e) is virtually perfect, showing distortion only due to statistical noise and the smoothing that results from a point-response-function with a two-pixel radius. The text describes how the basic structure in (e) can be guessed from the information in (c) or (d). In (f), $B(x,y)$ is displayed with a look-up-table that emphasizes low-amplitude noise structure.

this case, the fact that p is wider at $\phi=0$ than at $\phi=\pi/2$ in Figs. 5(c) and 5(d) means that B has a larger extent in the x direction than in the y direction. The four narrow bright features at $\phi=0$, and the way each one has a width that varies sinusoidally with ϕ, tell us there are four short vertical lines in B. Similarly, the existence and position in B of a short horizontal line segment and two diagonal segments can be
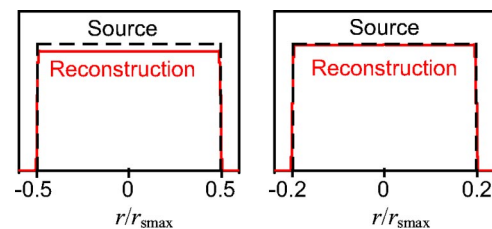

FIG. 6. (Color online) Values along the diameters of reconstructed uniform disks with $r_s=0.5r_{smax}$ and $r_s=0.2r_{smax}$, compared with the original source functions. The reconstructions were calculated from analytically simulated penumbral data with no noise. Reconstruction errors scale with $(r_s/r_{smax})^2$, and are completely negligible in the context of data taken on OMEGA (where r_s is typically smaller than $0.05r_{smax}$).

ascertained from the locations of their projections in Figs. 5(c) and 5(d).

C. Point-response function, spatial resolution, and noise

The spatial resolution of surface-brightness reconstructions is limited by the smoothing used to reduce noise from counting statistics. We use $F_{smooth}(r) = \pi^{-1/2} r_{prf}^{-1} e^{-(r/r_{prf})^2}$ in Eq. (6), resulting in a point response function for the reconstructed $B(x,y)$ with the form $e^{-(x^2+y^2)/r_{prf}^2}$; the radius r_{prf} is specified by the user in order to achieve a desired noise reduction. This results in a well characterized and well behaved point-response function as well as noise of predictable character. The resolution can be characterized by r_{prf} or by the full width at half maximum, which is $1.66 r_{prf}$.

The signal-to-noise ratio of a reconstructed surface brightness image can now be studied. The "signal" is just the true surface brightness with a small modification for effects of smoothing. For Gaussian surface brightness distributions, which are often observed (see Sec. IV), the peak value is

$$\text{Signal} = \frac{Y_s}{\pi(r_s^2 + r_{prf}^2)} \mu m^{-2}, \tag{8}$$

where r_s is the radius at which the brightness is e^{-1} times the peak value. The point-response function broadens the brightness distribution without changing the total yield, resulting in reduced central image brightness. Equation (8) is approximately correct for a uniform-brightness disk of outer radius r_s, although the effect of r_{prf} is then not exact. The rms noise amplitude in the image can be shown[48] to be

$$\text{Noise} \approx \left[0.4 \left(\frac{M+1}{M} \right)^{1/2} \frac{L}{R_a^{1/2}} \right] r_{prf}^{-5/2} Y_s^{1/2} \mu m^{-2}. \tag{9}$$

[Equation (9) assumes all detector events are from signal protons. If there is a uniform background of $N_{background}$ spurious tracks per unit area on the detector, then Y_s is replaced by $Y_s + 8\pi(M+1)^2 L^2 N_{background}$.] The ratio of Eqs. (8) and (9) gives the signal-to-noise ratio (SNR)

$$\text{SNR} \approx \left[0.8 \left(\frac{M}{M+1} \right)^{1/2} \frac{R_a^{1/2}}{L} \right] \frac{r_{prf}^{5/2}}{(r_s^2 + r_{prf}^2)} Y_s^{1/2}. \tag{10}$$

The noise has several important features. First, its amplitude depends only on source yield; it is independent of source size and shape. Second, noise in the reconstructed image is not "white;" its amplitude goes as the square of frequency.[48] Third, this frequency dependence tends to make the noise look "lumpy," being completely dominated by the highest frequencies allowed by the smoothing. Fourth, the noise is roughly homogeneous and isotropic, at least out as far as this reconstruction algorithm is useful (say $r \lesssim 0.7 r_{smax}$). Several of these features can be seen in Fig. 5(f).

Equation (10) can be used to determine what kind of resolution is obtainable, if we assume that we want a SNR of 20 to get decent image clarity. Setting $\text{SNR} = 20$ and solving for r_{prf}, we find different behavior depending on whether we are asking for resolution in the sense of the width of a reconstructed delta-function source

$$r_{prf} \approx \left[25 \left(\frac{M+1}{M} \right)^{1/2} \frac{L}{R_a^{1/2}} \right]^2 Y_s^{-1}, \quad r_s \ll r_{prf}, \tag{11}$$

or the more realistic resolution for structure on a scale smaller than the overall source size

$$r_{prf} \approx r_s^{4/5} \left[25 \left(\frac{M+1}{M} \right)^{1/2} \frac{L}{R_a^{1/2}} \right]^{2/5} Y_s^{-1/5}, \quad r_s \gg r_{prf}. \tag{12}$$

D. Predicted real-world performance at OMEGA

Numbers relevant to experiments at OMEGA, calculated from the dimensions in Fig. 2(a), are

$$\text{SNR} \approx 20 \left(\frac{r_{prf}}{10 \ \mu m} \right)^{5/2} \frac{(30 \ \mu m)^2}{(r_s^2 + r_{prf}^2)} \left(\frac{Y_s}{10^{10}} \right)^{1/2} \tag{13}$$

and (for r_{prf} smaller than r_s)

$$r_{prf} \approx 10 \left(\frac{Y_s}{10^{10}} \right)^{-1/5} \left(\frac{r_s}{30 \ \mu m} \right)^{4/5} \mu m. \tag{14}$$

Typical OMEGA implosions of D^{3}He-filled capsules with thick CH shells have $r_s \sim 30 \ \mu m$ and $Y_s \sim 10^9$, leading us to a predicted resolution of $r_{prf} \approx 16 \ \mu m$.

IV. RADIAL BURN PROFILE RECONSTRUCTION

When implosions are nearly spherical, there are advantages to pursuing a different approach: the structure of the penumbra, averaged over ϕ, can be used to estimate the radial profile of the burn in D^{3}He reactions per unit volume. This requires going from the approximate straight-line-integral projection $P(r)$ to $B(r)$ via Abel inversion, and then going from $B(r)$ to $S(r)$ via another Abel inversion. To obtain as much information as possible about the basic size and shape of $S(r)$ while minimizing the effects of noise, we apply this approach by using a family of simple radial functions for $S(r)$ that have analytic counterparts for straight-line-integral projections. This is the family of powers α of a parabola. Defining a "peakedness" parameter $\beta \equiv \alpha/(\alpha+1)$, it can be shown that if

$$S(r) = \frac{\pi A}{(1-\beta) r_1^2} \left[1 - \left(\frac{r}{r_1} \right)^2 \right]^{\beta/(1-\beta)}, \tag{15}$$

then the equivalent straight-line projection is

$$P(r) = A \left[1 - \left(\frac{r_0 - r}{M r_1} \right)^2 \right]^{1/(1-\beta)}. \tag{16}$$

As illustrated in Fig. 7, $\beta = 0$ corresponds to a flat source. Increasing β makes the source more peaked; in the limit $\beta = 1$, expressions (15) and (16) both become Gaussians. Decreasing β below 0 makes the source increasingly hollow. In practice, a least-squares fit is used to find the parameters r_0, A, r_1, and β in Eq. (16) [the origin used for binning $N(r,\phi)$ is determined by minimizing the best-fit value of r_1]; $S(r)$ is then determined directly from Eq. (15). There are two advantages to this approach. First, the results are local total emission values and not projections. Second, the least-squares fit can be performed without doing very much smoothing of dN/dr; the result is a more accurate measure-
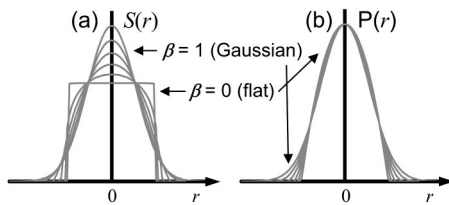
FIG. 7. Families of functions described in Sec. IV. (a) Radial profiles of spherically symmetric, three-dimensional sources, with "peakedness" β varying from 0 to 1. (b) Corresponding shapes of one-dimensional, straight-line projections of the surface brightness distribution. Negative values of β can also be used.

ment of the source size than can be obtained through two-dimensional (2D) reconstruction. Most data analyzed thus far for D³He-filled capsules have been compatible with radial profiles of Gaussian shape.

V. DISCUSSION

The instrumentation and algorithms described above have been successfully applied to a wide range of experiments at OMEGA. The method of Sec. IV has been used to find clear trends in the variation of burn-region size with capsule type (fill pressure, shell material and thickness) and laser conditions (energy and smoothing).[35] These results are particularly important for studying mix and for benchmarking the numerical simulations. The 2D reconstruction techniques have recently been used to study the relationship between laser drive asymmetry and burn asymmetry. Those measurements are being combined with measurements of areal density asymmetry, burn time evolution, and x-ray emission asymmetry; specific results of these experiments, comparisons with simulations, and physics analysis, will be described elsewhere.

[1] J. D. Lindl, R. L. McCrory, and E. M. Campbell, Phys. Today **45**, 32 (1992).
[2] J. D. Lindl, *Inertial Confinement Fusion* (Springer-Verlag, New York, 1999).
[3] S. W. Haan, Stephen M. Pollaine, John D. Lindl *et al.*, Phys. Plasmas **2**, 2480 (1995).
[4] F. J. Marshall, J. A. Delettrez, R. Epstein *et al.*, Phys. Plasmas **11**, 251 (2004).
[5] K. A. Nugent and B. Luther-Davies, Opt. Commun. **49**, 393 (1984).
[6] K. A. Nugent and B. Luther-Davies, J. Appl. Phys. **58**, 2508 (1985).
[7] K. A. Nugent and B. Luther-Davies, Appl. Opt. **25**, 1008 (1986).
[8] K. A. Nugent and B. Luther-Davies, J. Appl. Phys. **60**, 1289 (1986).
[9] K. A. Nugent, Opt. Commun. **62**, 1658 (1988).
[10] K. A. Nugent, Rev. Sci. Instrum. **59**, 1234 (2003).
[11] D. Ress, R. A. Lerche, R. J. Ellis, S. M. Lane, and K. A. Nugent, Science **241**, 956 (1988).
[12] D. Ress, R. A. Lerche, R. J. Ellis, S. M. Lane, and K. A. Nugent, Rev. Sci. Instrum. **59**, 1694 (1988).
[13] D. Ress, IEEE Trans. Nucl. Sci. **37**(2), 155 (1990).
[14] N. Miyanaga, Y.-W. Chen, M. Unemoto *et al.*, Rev. Sci. Instrum. **61**, 3230 (1990).
[15] R. A. Lerche, D. Ress, R. J. Ellis, S. M. Lane, and K. A. Nugent, Laser Part. Beams **9**, 99 (1991).
[16] R. K. Fisher, R. B. Stephens, L. Disdier *et al.*, Phys. Plasmas **9**, 2182 (2002).
[17] R. A. Lerche, N. Izumi, R. K. Fisher *et al.*, Rev. Sci. Instrum. **74**, 1709 (2003).
[18] J. P. Garconnet, O. Delage, D. Schirmann *et al.*, Laser Part. Beams **12**, 563 (1994).
[19] O. Delage, J.-P. Garconnet, D. Schirmann, and A. Rouyer, Rev. Sci. Instrum. **66**, 1205 (1995).
[20] G. L. Morgan, R.R. Berggren, P. A. Bradley *et al.*, Rev. Sci. Instrum. **72**, 865 (2001).
[21] Alain Rouyer, Rev. Sci. Instrum. **74**, 1234 (2003).
[22] L. Disdier, A. Rouyer, A. Fedotoff *et al.*, Rev. Sci. Instrum. **74**, 1832 (2003).
[23] D. C. Wilson, C. R. Christensen, G. L. Morgan *et al.*, Rev. Sci. Instrum. **74**, 1705 (2003).
[24] C. R. Christensen, Cris W. Barnes, G. L. Morgan, M. Wilke, and D. C. Wilson, Rev. Sci. Instrum. **74**, 2690 (2003).
[25] C. R. Christensen, D. C. Wilson, Cris W. Barnes *et al.*, Phys. Plasmas **11**, 2771 (2004).
[26] M. J. Moran, S. W. Haan, S. P. Hatchett *et al.*, Rev. Sci. Instrum. **74**, 1702 (2003).
[27] R. D. Petrasso, C. K. Li, M. D. Cable *et al.*, Phys. Rev. Lett. **77**, 2718 (1996).
[28] F. H. Séguin, C. K. Li, J. A. Frenje *et al.*, Phys. Plasmas **9**, 2725 (2002).
[29] F. H. Séguin, C. K. Li, J. A. Frenje *et al.*, Phys. Plasmas **9**, 3558 (2002).
[30] C. K. Li, F. H. Séguin, J. A. Frenje *et al.*, Phys. Rev. Lett. **92**, 205001 (2004).
[31] F. H. Séguin, J. R. Rygg, J. A. Frenje *et al.*, Bull. Am. Phys. Soc. **48**, 57 (2003).
[32] J. A. Frenje, C. K. Li, F. H. Séguin *et al.*, Phys. Plasmas **11**, 2480 (2004).
[33] V. Yu. Glebov *et al.* (submitted).
[34] F. H. Séguin, J. A. Frenje, C. K. Li *et al.*, Rev. Sci. Instrum. **74**, 975 (2003).
[35] J. L. DeCiantis *et al.* (to be submitted).
[36] Y.-W. Chen, M. Yamanaka, N. Miyanaga *et al.*, Opt. Commun. **73**, 227 (1989).
[37] M. Nakai, M. Yamanaka, H. Azechi *et al.*, Rev. Sci. Instrum. **61**, 3235 (1990).
[38] A. P. Fews, M. J. Lamb, and M. Savage, Opt. Commun. **94**, 259 (1992).
[39] A. P. Fews, M. J. Lamb, and M. Savage, Opt. Commun. **98**, 159 (1993).
[40] A. P. Fews, M. J. Lamb, and M. Savage, Laser Part. Beams **12**, 1 (1994).
[41] A. P. Fews, P. A. Norreys, F. N. Beg *et al.*, Phys. Rev. Lett. **73**, 1801 (1994).
[42] T. R. Boehly, D. L. Brown, R. S. Craxton *et al.*, Opt. Commun. **133**, 496 (1997).
[43] R. L. Fleischer, P. B. Price, and R. M. Walker, *Nuclear Tracks in Solids, Principles and Applications* (University of California Press, Berkeley, CA 1975).
[44] A. P. Fews, Nucl. Instrum. Methods Phys. Res. B **71**, 465 (1992).
[45] J. Radon, Ber. Verh. Saechs. Akad. Wiss. Leipzig, Math.-Naturwiss. Kl. **69**, 262 (1917), reprinted in S. Helgason, *The Radon transform* (Progr. Math., 5, Birkhäuser, Boston, 1980).
[46] L. A. Shepp and B. F. Logan, IEEE Trans. Nucl. Sci. **21**, 21 (1974).
[47] Z. H. Cho, J. P. Jones, and M. Singh, *Foundations of Medical Imaging* (Wiley, New York, 1993).
[48] We can see why the SNR of an azimuthally symmetric B has the form shown in Eq. (10) by evaluating Eq. (1) at the origin: $B(0,0) \approx -[4\pi M(M+1)^2 L^2][F_{smooth}*h_{CT}*dN(r)/dr]_{r=r_0}$ (ignoring small corrections due to $C(r)$ and the small term proportional to r_{rsmax}^{-2}). For B to have an effective resolution element of size D, F_{smooth} must have the effect of binning $N(r)$ in radial intervals of width MD. The number of protons in one bin near $r=r_0$ can be seen from geometry to be $N_t = [0.25M/(M+1)](R_a/L^2)DY_s$, so the SNR of $N(r)$ at $r=r_0$ is $N_t^{1/2}$. The effect of the convolution filter h_{CT} is to weight spatial structure inversely with wavelength; the same is true of the radial derivative. The SNR of B is therefore proportional to $(D/r_s)^2 N_t^{1/2}$, which has the same form as Eq. (10) for $D \ll r_s$. The value of the constant of proportionality for Gaussian smoothing, and numerical verification of the scaling with geometric parameters, can be demonstrated using Monte-Carlo-simulated data.